ELSEVIER

NDT&E International 35 (2002) 301–316

NDT&E international

www.elsevier.com/locate/ndteint

Experimental crack identification using electrical impedance tomography

R. Lazarovitch, D. Rittel*, I. Bucher

Faculty of Mechanical Engineering, Technion, Israel Institute of Technology, Technion City, 32000 Haifa, Israel

Received 21 June 2001; revised 19 October 2001; accepted 21 October 2001

Abstract

This paper addresses the problem of practical crack identification in electrically conducting specimens using *only* boundary measurements. The method is commonly referred to in the literature as Electrical Impedance Tomography (EIT).

Crack identification is determined from the electrical impedance distribution, which amounts to solving an inverse problem, starting from boundary measurements. Whereas this kind of inverse problem has been extensively addressed in its theoretical and numerical aspects, there is a scarcity of *experimental* results aimed at examining the applicability of the method for real conditions.

We present new experimental results, based on a simple identification methodology. The efficiency and limitations of this method are assessed through a series of numerical simulations and laboratory experiments on two-dimensional geometries. Following a preliminary numerical validation stage, actual crack detection is carried out on a discrete network of resistors, as an approximation to Laplace's equation. Next, experiments are carried out on a continuous conductive medium, containing one and two flaws. Our results show that EIT is a promising candidate for crack identification in real life conditions with a potential for multiple crack detection.

Keywords: Conductance; Computational algorithm; Homogeneous medium

1. Introduction

Non Destructive Testing (NDT), is concerned with the detection of hidden structural flaws, without damaging the surface or functionality of the structure. Some of the most common NDT methods are based on visualization of the flaws by means of various techniques, such as dye penetrants, magnetic particles, eddy current, ultrasonic and radiographic [1].

This paper deals with another NDT method called Electrical Impedance Tomography (EIT). The principle of EIT is related to the alteration of electrical conductance caused by a flaw. EIT is practically implemented on a (flaw containing) specimen by mapping its outer surface with electrodes, applying voltage on a couple of electrodes (or more) and measuring the resulting electrical potential on every one of the other electrodes. Processing the measured values by an appropriate algorithm (solution of the inverse problem) will result in a conductance distribution map, which should indicate the presence and location of the flaw in the specimen (Fig. 1).

The main advantages of EIT are the ability to identify cracks in geometrically complex structures, thus potentially providing a low cost, mobile and effective diagnosis tool. The main disadvantages of the method are its relatively low spatial resolution and its limitation to electrically conducting specimens. Other potential applications of EIT include medical tomography, imaging multiphase fluid flow and geophysics.

Several algorithms for the solution of the inverse problem at hand can be found in the literature [2–9]. Most of the papers address full field imaging by means of an impedance camera, rather than the detection of a single crack in the domain. Typical applications include the detection of corrosion damage [10,11] and geophysical problems [12].

Santosa and Vogelius [3] have developed a computational algorithm for the identification of a linear crack in a two-dimensional (2D) domain. This algorithm is based on a variation of Newton's method. It iteratively updates the location of the input voltage electrodes to achieve maximal sensitivity.

Liepa et al. [13] describes a 'Backprojection Imaging Algorithm', which was first developed by Barber and Brown [14]. It is described in detail in Ref. [15]. This method is reported as having a relatively low resolution. Therefore, its result is usually used as an input for a more accurate method (like the earlier-mentioned 'Computational Algorithm'). The technique relies on a large number of potential measurement sets made systematically. Every set

* Corresponding author. Tel.: +972-4829-3261; fax: +972-4832-4533.
E-mail address: merittel@tx.technion.ac.il (D. Rittel).

0963-8695/02/$ - see front matter
PII: S0963-8695(01)00054-8

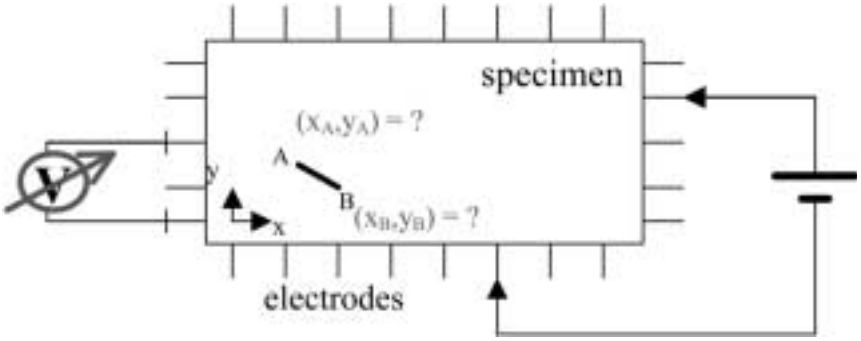

Fig. 1. Schematic description of EIT system.

produces a conductance distribution map. A superposition of every one of those maps is used to reconstruct a global distribution map for the whole domain. Liepa et al. [13] describes a 2D laboratory experiment, which consists of a cylindrical tank with 12 vertical electrodes inside. The tank was filled with an electrolyte simulating a homogeneous medium. A crack discontinuity was introduced by placing a metal strip vertically inside the tank. The results of this experiment were satisfactory. However, no experiment was carried out with an actual crack.

Mellings and Aliabadi [6] guess an initial crack location inside a 2D domain. This location is characterized by four design variables of the coordinates from its two ends. The Dual Boundary Element Method [16] is used to calculate the potential on the boundary induced from this crack location. Measurements are obtained from a real experiment. From the difference between calculated and measured potentials, an error function is generated. The location of the crack is assessed through an iterative minimization procedure of this error function.

Dines and Lytle [12] investigate numerically a 2D heterogeneous medium, which is modeled as a network of resistors. This network serves as a discrete approximation to the real domain [17]. Voltage is applied to the peripheral nodes, and the resulting node currents are measured. An iterative process is applied in order to reconstruct the variation of electrical conductivity inside the domain.

It can be seen from this brief survey, that in contrast with the large number of analytical and numerical studies, there is a scarcity of experimental work to assess the practical applicability of the method. One characteristic application was the use of EIT for medical purposes [18], produced by Barber and Brown [14,19].

Our paper deals with a 2D problem of crack identification.

In this work, we assess the applicability of EIT as an efficient tool for crack identification under realistic experimental conditions. The paper is organized as follows: first, a short statement of the problem at hand is given. Next, we present our methodology to identify cracks, including the description of the procedure to solve the inverse problem. Then, we report three distinct kinds of experiments (one numerical, two physical) aimed at assessing the applicability of our methodology. The main results of these experiments are discussed in view of the practical achievements of EIT for crack identification.

2. Statement of the problem

The electrical potential distribution inside a 2D conducting domain Ω with a perfectly insulating crack σ at steady state (Fig. 2), can be described by Laplace equation:

$$\nabla(\rho \nabla V) = 0 \qquad \text{in} \qquad \Omega \tag{1}$$

where $\rho(x, y)$ is the conductance distribution within the domain and $V(x, y)$ is the electrical potential distribution inside the domain. The boundary conditions are given by:

$$\rho \frac{\partial V}{\partial n} = 0 \qquad \text{on} \qquad \sigma \tag{2}$$

$$V = U \qquad \text{on} \qquad \partial\Omega \tag{3}$$

Eq. (2) is the Neuman boundary condition meaning that no current is going through the crack, and Eq. (3) is the Dirichlet boundary condition meaning that an outer potential U is applied on the domain boundary. The direct problem solves Eq. (1) for the potential V (inside the domain), given the boundary conditions and the conductance distribution ρ inside the domain. The inverse problem seeks to determine the distribution of

$$\rho = \rho(x, y),$$

given the boundary conditions and V on the external boundary only.

Inverse problem, such as the one dealt with here possess some inherent difficulties. According to Hadamard's definition, such problems may be ill posed problem and thus

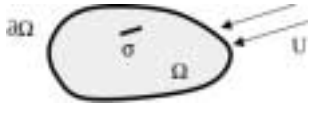

Fig. 2. Applying electrical potential on an object with internal crack.

would not always have a unique solution, and the solution. Furthermore, ill-posed problems give rise to a solution that does not depend continuously on the data [20]. The discontinuous dependence of the solution means that small errors in measurements may cause large errors in the solution. An additional characteristic of these problems is manifested by the fact that large changes inside the domain may be characterised by a very small effect on boundary measurements. The problem that is dealt with here shows some of the characteristics of an ill-posed problem as discussed above. Careful preparation of the experiment and handling of the data along with some redundancy of the provided data together with numerical safeguards, have all helped considerably in overcoming the ill-posedness of the problem.

3. Solution methodology

The proposed method here relies on the idealization of a continuous electrically conducting specimen as an array of resistors (Fig. 3). This equivalence, represented by a discrete network of resistors, can be illustrated by forming a finite difference approximation of Laplace's equation. Expanding Eq. (1) we obtain

$$\rho\nabla^2 V + \nabla\rho\nabla V = 0 \tag{4}$$

As a first approximation, we choose to neglect the second term in Eq. (4). Indeed, one can consider that everywhere *but* across the crack, both potential drops and resistance changes are small and continuous. The crack faces define an equipotential line with a resistivity jump. Yet, this assumption allows for a simple approximation of Eq. (4) as shown next. Using a finite difference expansion to obtain

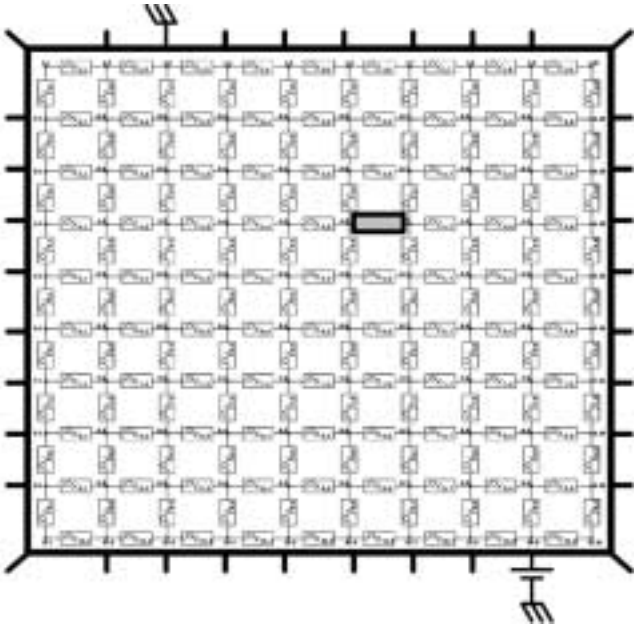

Fig. 3. Continuous domain represented as a network of resistors with an internal crack.

a central difference (h) of the second order [17], the approximated Eq. (4) at the point (x_k, y_k) is written as:

$$\rho\nabla^2 V \approx \frac{\rho}{h^2}(V(x_k + h, y_k) + V(x_k - h, y_k) + V(x_k, y_k + h) + V(x_k, y_k - h) - 4V(x_k, y_k)) = 0 \tag{5}$$

At this stage, one can note the similarity between Kirchoff's law applied to a network of resistors and Eq. (5), as shown in Appendix A. Now, for a network of resistors with m by n nodes, Kirchoff's law results in mn algebraic equations. In matricial representation, Kirchoff's law can be written as:

$$A_{mn\times mn}(\rho)V_{mn} = 0 \tag{6}$$

In the context of the direct problem, the unknown vector V is the electrical potential at every node in net. The matrix A, which is a function of the resistor values in the net, is singular. Here, the values of all the resistors composing the net are known. By applying an external voltage on two of the surrounding electrodes, we actually provide two boundary conditions to the problem, which are two of the mn values from vector V. Inserting these two known values into Eq. (6) yields:

$$\tilde{A}(\rho)\tilde{V} = B(\rho) \tag{7}$$

where, now $\tilde{A}_{(mn-2)\times(mn-2)}$ is no longer singular, thus we are able to solve

$$\tilde{V} = \tilde{A}^{-1}B \tag{8}$$

In the context of the inverse problem, let us denote the *unknown* parameters (having the physical units of conductance, i.e. 1/resistance) by:

$$\rho = \rho_1, \rho_2, \rho_3, \ldots, \rho_i, \ldots, \rho_N \tag{9}$$

where the number of resistors in the net is

$$N = m(n-1) + n(m-1) = 2mn - m - n \tag{10}$$

The solution of the direct problem will give the distribution of potentials:

$$\tilde{V} = \tilde{V}_1(\rho), \tilde{V}_2(\rho), \ldots, \tilde{V}_{mn-2}(\rho) \tag{11}$$

The number of nodes on the boundary is given by

$$mn - (m-2)(n-2) = 2m + 2n - 4 \tag{12}$$

Since we limit ourselves to measurements on the *sole* external boundary of the specimen, $\tilde{V}$ will now be reduced to $\hat{V}$, which consists of the boundary terms only. The objective is to determine a conductance distribution ρ, such that the vector of *calculated* potential values, from the direct problem solution model,

$$\hat{V} = \hat{V}_1(\rho), \hat{V}_2(\rho), \ldots, \hat{V}_k(\rho), \ldots, \hat{V}_{2m+2n-4}(\rho) \tag{13}$$

will be as close as possible to the vector of *measured*

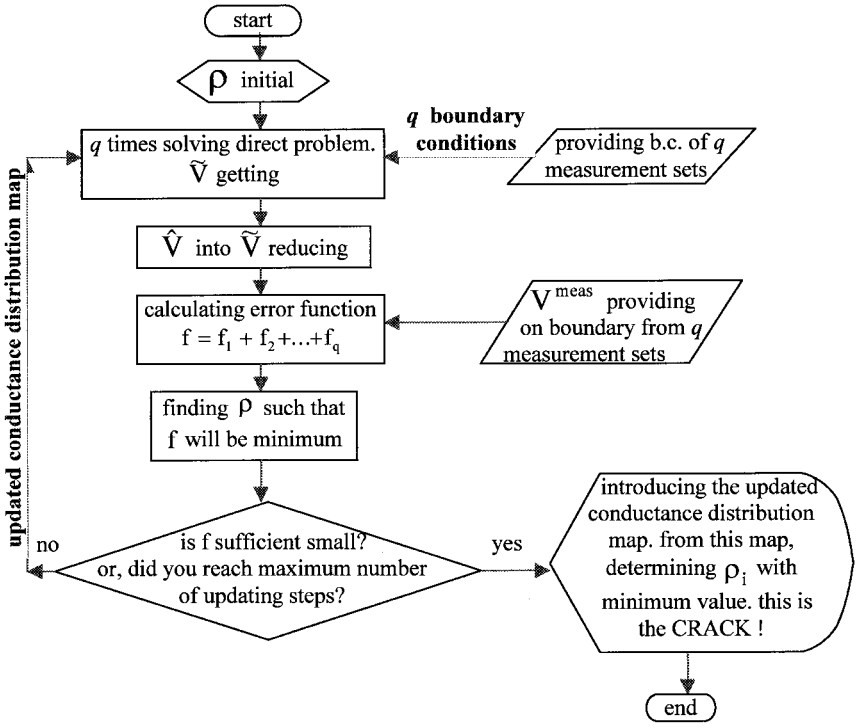

Fig. 4. Schematic description of crack identification procedure.

potential values from object's boundary

$$V^{\text{meas}} = V_1^{\text{meas}}, V_2^{\text{meas}}, \ldots, V_k^{\text{meas}}, \ldots, V_{2m+2n-4}^{\text{meas}} \tag{14}$$

This requirement can be simply expressed by the statement:

find ρ such that $\hat{V}(\rho) \cong V^{\text{meas}}$

This statement amounts to minimizing the cost (error) function:

$$f(\rho) = \sum_{k=1}^{2m+2n-4} \left\| \hat{V}_k(\rho) - V_k^{\text{meas}} \right\|^2 \tag{15}$$

This operation yields N non linear equations with N unknown variables ρ_i ($N = 2mn - m - n$) :

$$\frac{\partial f(\rho)}{\partial \rho_i} = 2 \sum_{k=1}^{2m+2n-4} (\hat{V}_k(\rho) - V_k^{\text{meas}}) \frac{\partial \hat{V}_k(\rho)}{\partial \rho_i} = 0 \tag{16}$$

$i = 1, 2, \ldots, N$

Solving these N equations yields an updated conductance distribution map.

As could be seen, the error function we seek to minimize is highly non linear in the parameters. Thus, analytical solutions are quite difficult to obtain and we must resort to numerical tools.

The previous description is a single step in getting an updated temporary solution. The optimal solution is obtained through an iterative procedure based on the earlier-mentioned step, as shown in Fig. 4. This procedure is based on the algorithm of Mellings and Aliabadi [6] with the three following main distinctions: way of modeling the crack inside the domain, method for getting the calculated potentials, amount and type of the design variables (their value represents the updated crack location).

Steps towards overcoming the ill-posedness: It should be noted that we do not rely on a single measurement set only. Rather, in order to overcome the relative insensitivity to small conductance changes of the inverse problem at hand, we perform several measurement sets (q). The additional independent sets of measurements convert the initial problem from an under determined situation (where no unique solution can be obtained) into what seems to be a redundant and in fact an overdetermined problem. The additional data improves significantly the rate of convergence of the solution, at the cost of moderately slowing down the numerical procedure, but allowing us to progress towards a unique solution.

Some more improvement in the conditioning of the problem, is obtained by applying engineering judgment, such as directing the solution towards a reasonable solution area and on the other hand preventing it to continue running into a non reasonable convergence direction (like the boundary itself—see Fig. 10 and Appendix C.2). In addition, engineering judgment has been used to select the optimal location of the external voltage boundary conditions.

It should also be noted that we did not investigate the issue of non uniqueness mathematically, although we did it indirectly by performing numerical simulations and laboratory experiments as described in Section 4.

Fig. 5. Discrete domain experimental system.

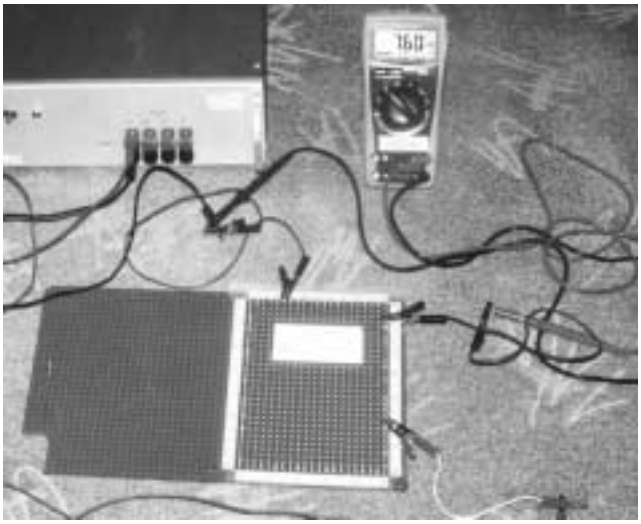

Fig. 6. Continuous domain experimental system.

4. Experimental

Three kinds of experiments were performed, as described below.

4.1. Numerical simulation

The efficiency of the proposed methodology was first verified by means of numerical simulations. A rectangular *discrete* domain (network of resistors), with a numerically generated crack (high resistance), was modeled. The convergence of the solution was monitored step by step.

4.2. Physical experiment 1—Network of resistors

In the second set of experiments, an experimental system was built from a network of resistors. In this system, all the resistors, but one, were identical. One of the resistors was arbitrarily assigned a higher resistance value. This resistor was representing the crack, as in the previous numerical experiment. Using a stabilized voltage source and a voltmeter, boundary potentials were determined for this network. The measured values were input into the earlier-mentioned solution algorithm, to identify the location of the cracked-equivalent resistor. The experimental setup is shown in Fig. 5.

4.3. Physical experiment 2—continuous domain

In this series of experiments, a continuous 2D rectangle made of (conductive) carbon paper was used. Around the domain a grid of regularly spaced metal screws were used to attach electrical terminals for setting various boundary conditions. A small incision was made on the carbon paper to replicate the crack. The reason for using a carbon paper instead of a metallic plate is because the resistance of this paper is much higher in comparison with metal and therefore smaller currents were needed and hence a standard voltage source could be used. The experimental setup is shown in Figs. 6 and 7.

5. Results

Throughout the experiments, there was a need to assess whether a sufficient number of iterations had been performed, along with the quality of the solution. Therefore, after each iteration, a crack identification factor (crack-factor) has calculated for each of the 'resistors' on the network, as follows

$$(\text{Crack-factor})_i = \frac{\rho_i}{\frac{1}{N}\sum_{a=1}^{N}\rho_a} \tag{17}$$

This factor allows us to differentiate each resistor from the others. The smallest value is assigned to the crack.

The numerical iterative solution as described earlier, is

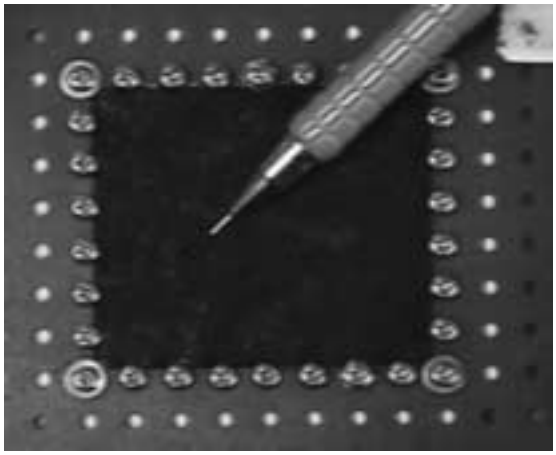

Fig. 7. Carbon paper with surrounding electrodes and internal crack (indicated).

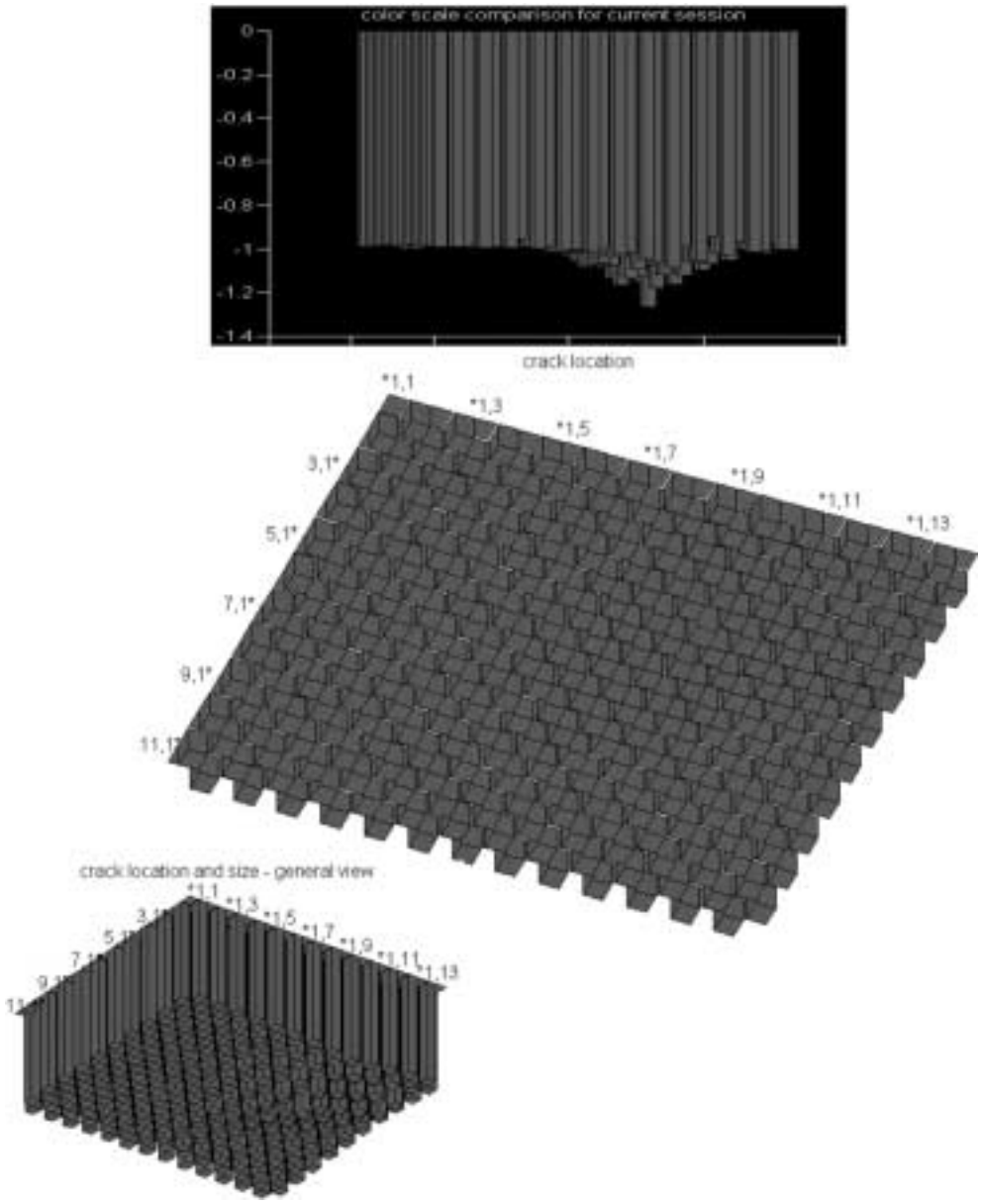

Fig. 8. Numerical simulation, 11×14 nodes, $q = 4$ measurement sets, crack at $\rho x 4, 9$. Solution displayed after 2000 optimization steps.

performed using Matlab [21] and Matlab Optimization Toolbox software [22]. In general, after providing an initial guess, we perform a constrained non linear optimization, using a mathematical algorithm based on the SQP (Sequential Quadratic Programming) method [23,24]. On every iteration step, we updated the variables (i.e. resistors) values using the BFGS algorithm [1,25].

Figs. 8–13 shows the results of the different experimental tests. Every figure features three different graphs containing bars, with height and color of which is a function of the resistors' crack-factor value, i.e.:

$$H_i = -\frac{1}{(\text{Crack-factor})_i} \tag{18}$$

The red bar indicates the resistor, which represents the crack. The graph called 'crack location' shows the whole net in isometric view. Row and column numbers (shown at row and column number one) serve to identify the nodes, which are represented as green–yellow squares. The relation between the node number and the name of its surrounding resistors is shown in Fig. 3.

Fig. 8 shows the results of a numerical simulation. The crack was located in $\rho_{x4,9}$ and was detected in the same location. Here, there is no experimental noise so that the simulation aims at reproducing 'perfect' conditions. The crack is clearly protruding and is surrounded by several resistors with a lower resistance value arranged in concentric circles (indicated by the color code). The results of this simulation clearly illustrate the capability of our algorithm to process boundary voltages in order to properly identify the crack.

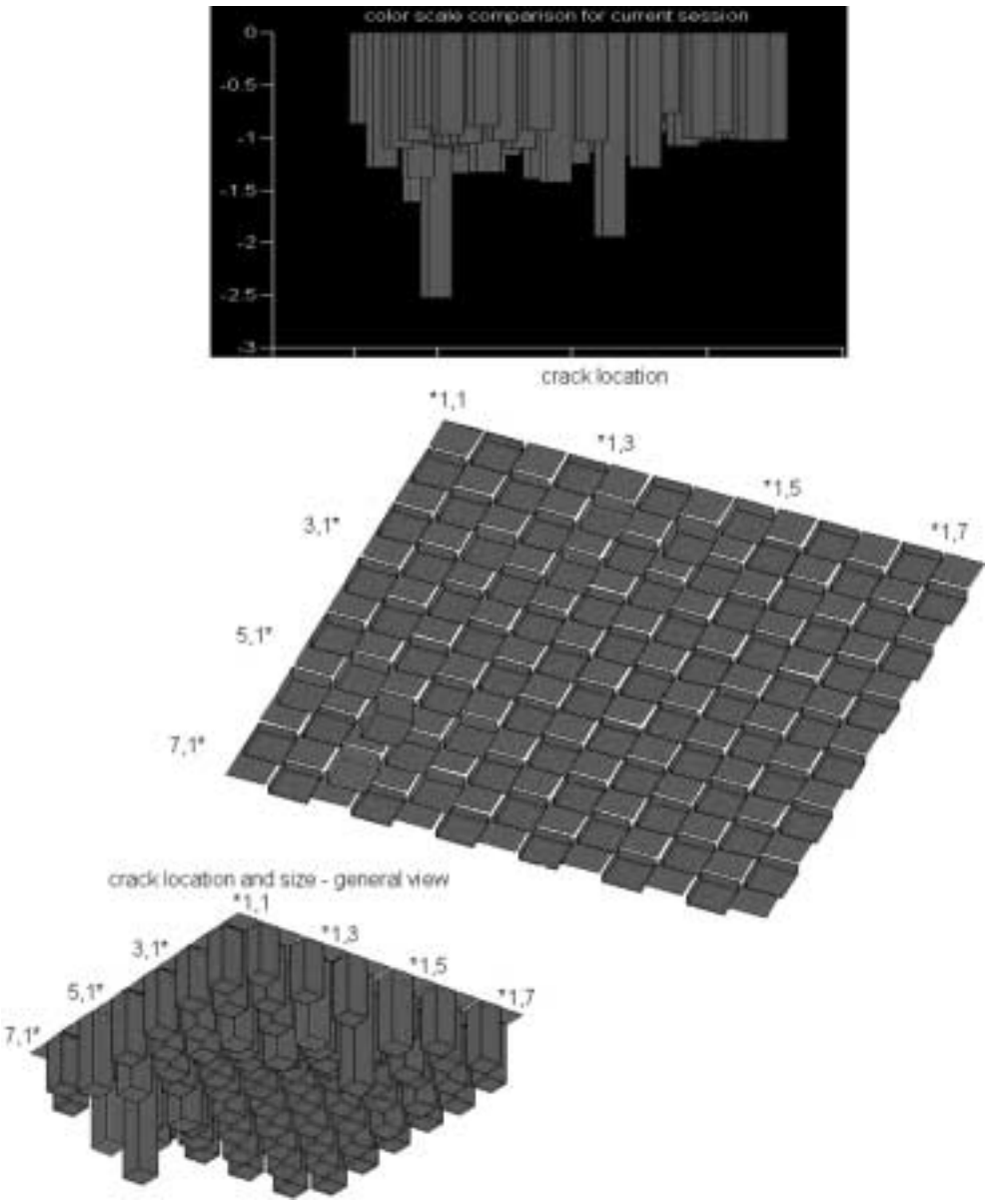

Fig. 9. Discrete domain, 7×7 nodes, $q = 3$ measurement sets, crack at $\rho y5,2$. Solution displayed after 350 optimization steps.

Fig. 9 shows the results for a discrete domain, i.e. a network of resistors. The crack was located in $\rho_{y5,2}$. The detected crack location, shown in red, corresponds exactly to the actual crack location. Several experiments of this kind were performed, and in each case the crack was located with the same degree of accuracy.

Fig. 10 shows the results for a continuous carbon paper. The crack appears clearly at $\rho_{x6,6}$. This location is very close to the actual crack location, $\rho_{x5,6}$. However, in this experiment, several 'potential' cracks are detected in the vicinity of this crack. In other words, the determination appears to be more ambiguous than in the two previous examples.

Consequently, the quality of the results obtained through the identification procedure was assessed for a reference experimental test on a discrete domain, in which no crack has been introduced. As shown in Fig. 11, none of the resistors protrude. The algorithm thus works properly, without introducing artifacts that might lead to erroneous conclusions about the presence of a crack.

Fig. 12 shows preliminary results for a multiple crack case (2 cracks: $\rho_{x5,4}$ and $\rho_{y2,6}$). It can be noted that the algorithm could correctly identify the cracks (in red). However, the contrast due to the cracks is not quite strong. Consequently, the same case was processed with a larger number of optimization steps. As shown in Fig. 13, the height of red bars indicating the cracks has noticeably increased with respect to that shown in Fig. 12. This result is definitely promising.

6. Discussions

A simple representation of a conducting domain

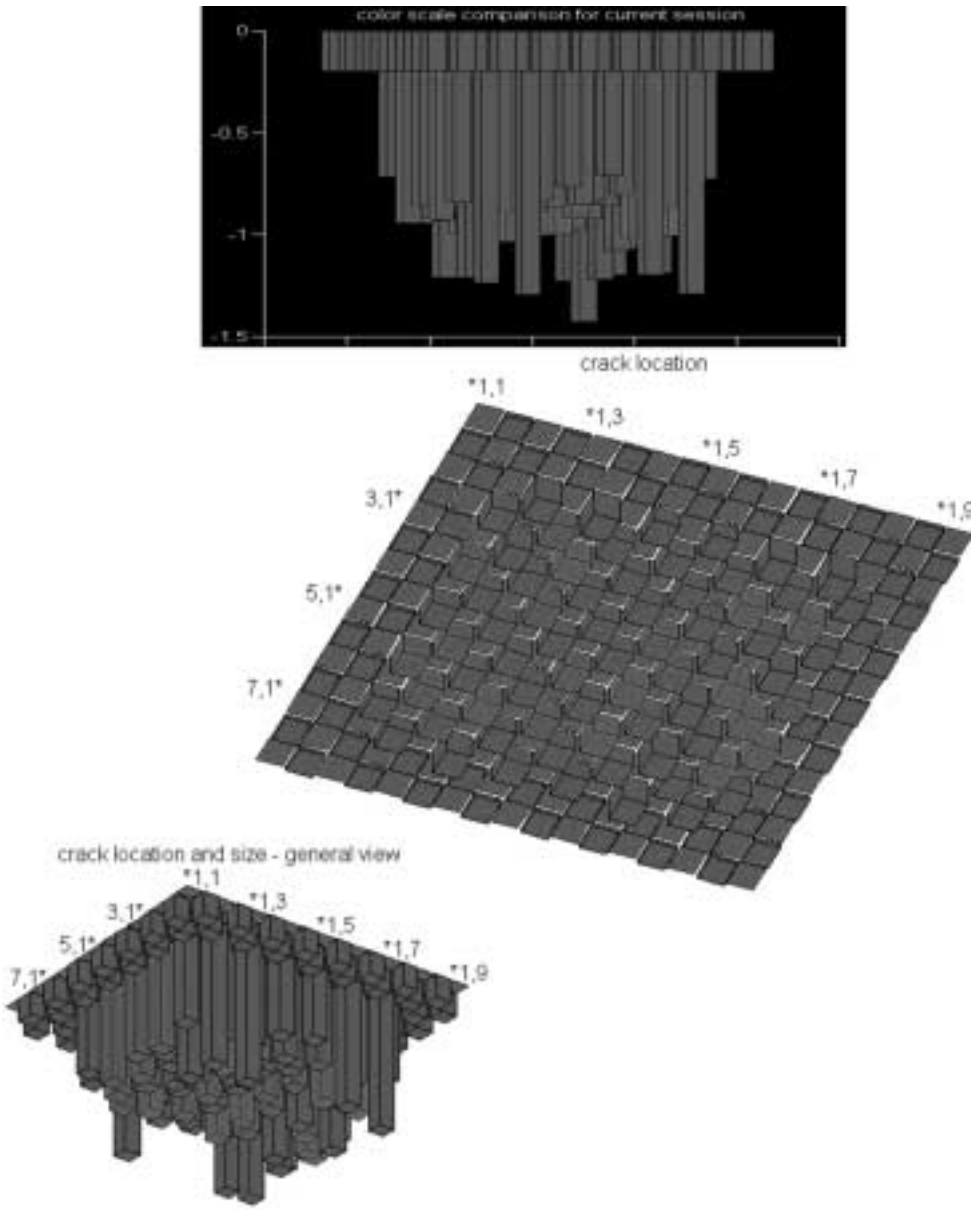

Fig. 10. Continuous domain, 8×9 nodes, $q = 5$ measurement sets, crack at $\rho x 5, 6$. Solution displayed after 2000 optimization steps.

having one (or more) embedded crack was presented in this paper. This is based on a simplified representation of Laplace equation, which is subsequently discretized for solution. This approach has been used in the past [17] and used successfully for numerical simulations [12]. Crack identification was achieved, based on the repeated minimization of a cost function. This approach has been tested and successfully validated numerically and experimentally.

As a first remark, one should note that the use of numerical methods, such as finite element solution, has been deliberately avoided. The reason is that we did not want to introduce additional numerical noise related to the domain discretization procedure and associated sensitivity to the selected mesh. The objective was to keep a single fixed mesh for all the iterations, to allow for comparison between the different cases examined in this work. It can be noted that Dines and Lytle [12] adopted a similar approach in their numerical investigation of the conductance problem.

The numerical simulation shows that a simple algorithm, such as the one presented here, is sufficient to identify a crack using EIT. This algorithm has by no means been optimized and just serves as a basic identification tool. The limitations of this detection technique should be further assessed. More sophisticated approaches, such as shown in Section 1, would most likely accelerate the rate of convergence of the identification process.

The *experimental* results are original in the sense that such results have not been reported previously, to the best

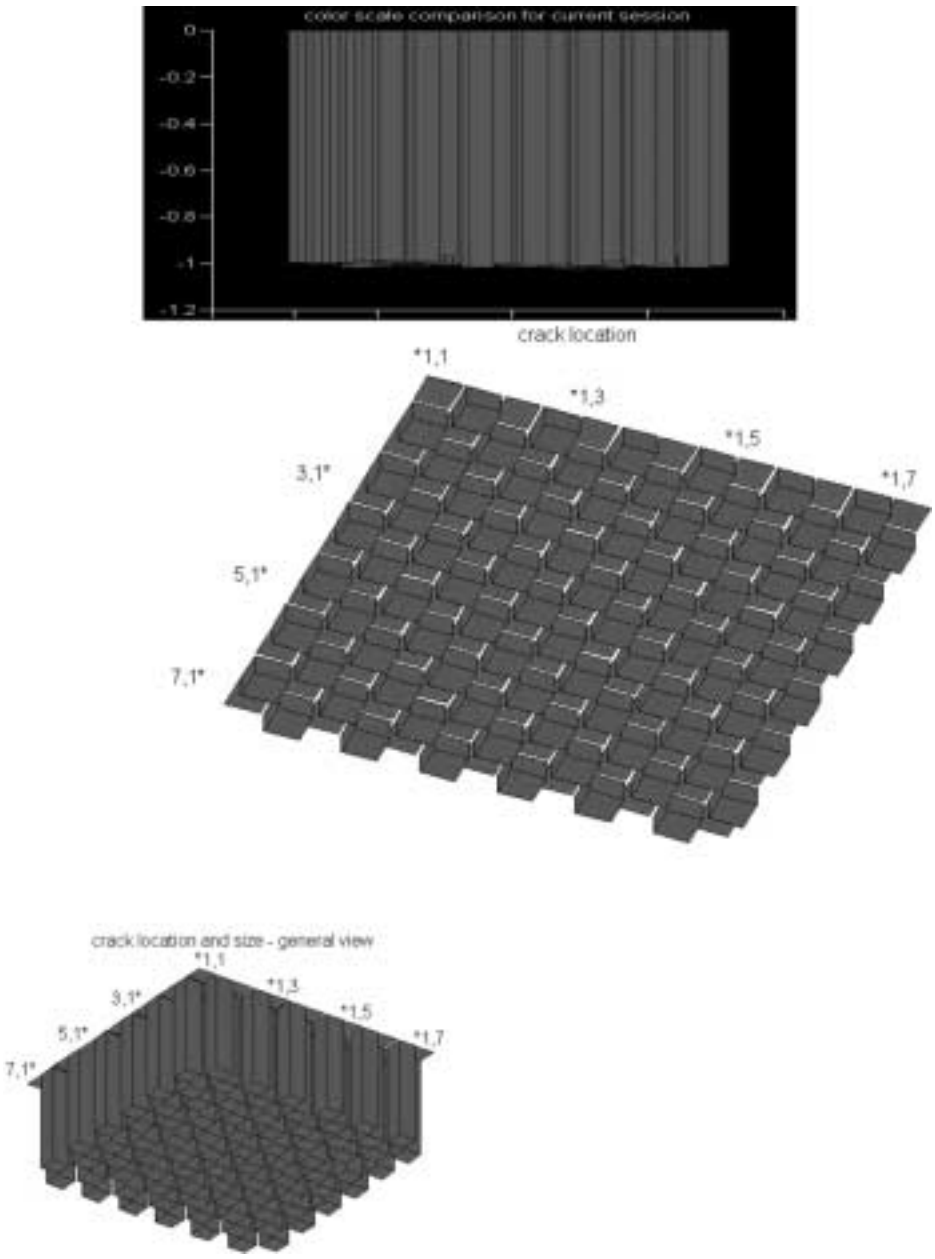

Fig. 11. Reference experimental test on domain without crack inside it, $q = 3$ measurement sets. Solution displayed after 350 optimization steps.

of the authors' knowledge. These experiments show the feasibility of EIT in real life conditions, which include the inherent experimental noise and fluctuations.

It can also be noted that, despite its simplicity, the adopted methodology introduces no artifacts. In other words, fictitious (non existent) cracks were not detected. The cracks were identified unambiguously, for the network of resistors, and quite clearly for the continuous medium, provided a sufficient number of iterations.

For the continuous medium, the simple discretization scheme employed here yield valuable results, for which the quality improves with the number of iteration steps. The lower resolution is explained due to the ill-posedness of the inverse problem. In these experiments, we noted that the location of external voltage boundary conditions is very important and could greatly affect the quality of the reconstructed solution. Moreover, we also observed that increasing the number of measurement sets improves the numerical convergence. Increasing the number of optimization steps produces a clear and better solution, while increasing the number of 'resistor' elements and number of electrodes on boundary would produce a solution with higher resolution, even though this may cause numerical difficulties and relatively slow convergence.

It thus seems that future work should concentrate on the following issues:

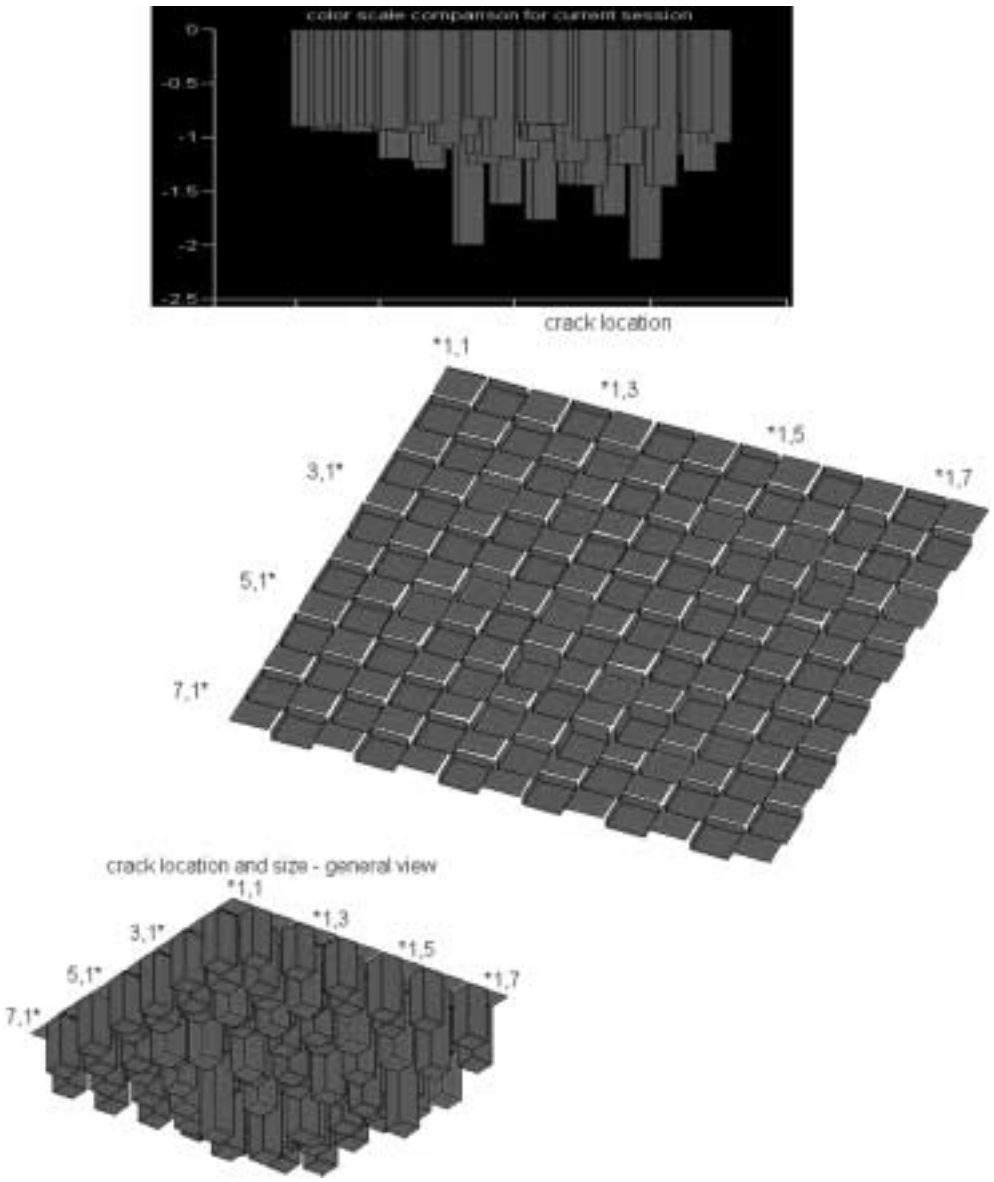

Fig. 12. Multiple cracks case, $q = 4$ measurement sets, cracks at $\rho x5, 4$ and $\rho y2, 6$. Solution displayed after 100 optimization steps.

- Improving the numerical algorithm.
- Investigating the minimum number of measurement sets (q) and their minimum requirements for distribution on boundary needed to identify cracks.
- Investigating the sensitivity of crack identification using the algorithm presented here.
- Quantify the values of some parameters mentioned in this paper needed for identifying a crack.
- Extending the problem to identify cracks on a 3D object (see Appendix B).

7. Conclusions

- A simple methodology for practical identification of cracks using EIT has been presented and validated experimentally.
- Crack identification is achieved by solving the inverse problem, which consists of determining the distribution of electrical conductance of a medium from boundary measurements. The problem is solved by minimizing a cost function, which expresses the difference between measured and calculated boundary potentials.
- The tendency towards ill-posedness of this inverse problem was overcome by:
  (a) enriching the boundary measurements using a succession of independent experiments,
  (b) careful calibration of the measurements,
  (c) applying some regularization means in the numerical step as a safeguard against divergence.
- The approach has been implemented practically in three

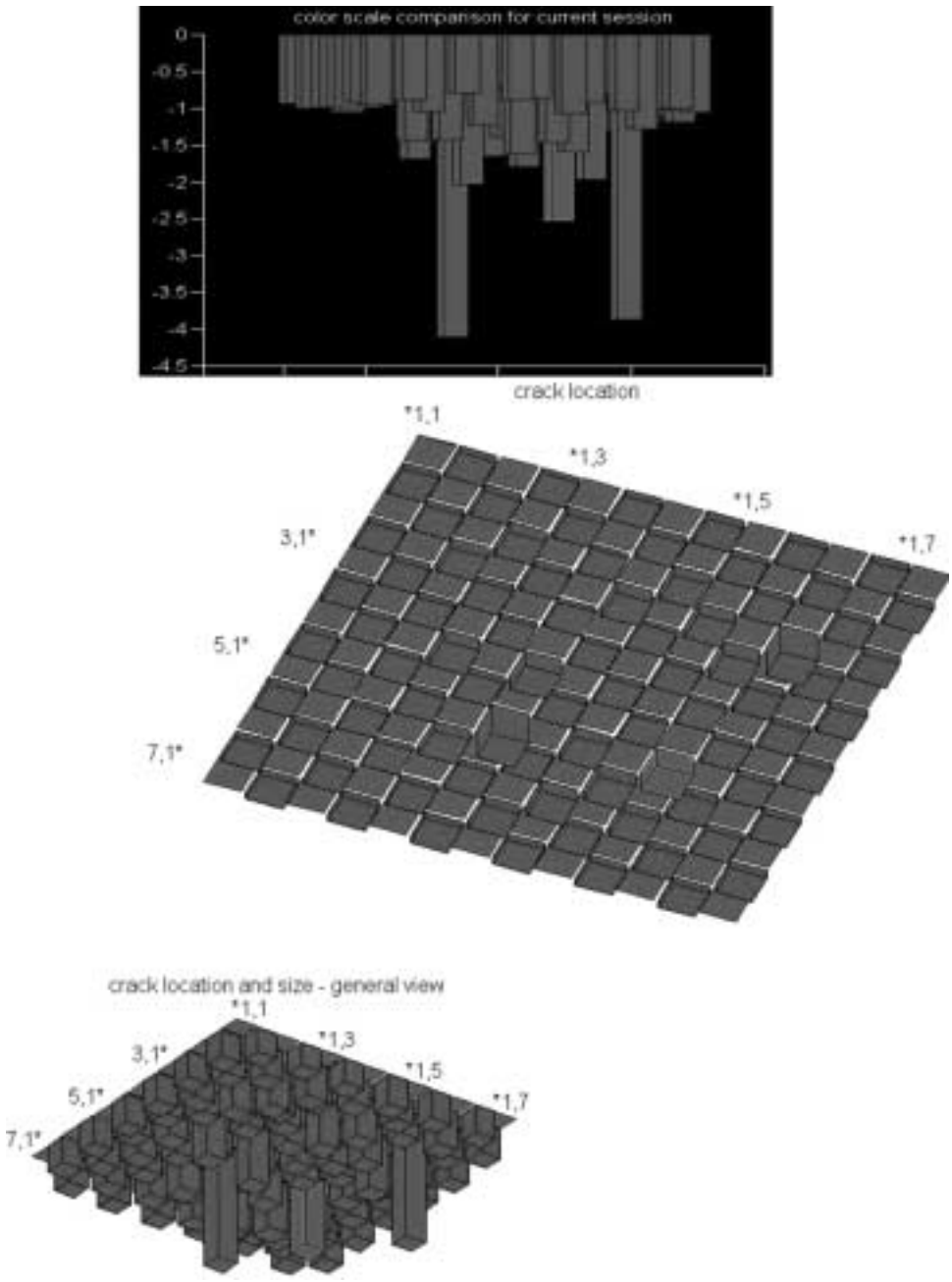

Fig. 13. Multiple cracks case, identical to Fig. 12, but solution displayed after 300 optimization steps.

distinct kinds of experiments: numerical, network of resistors (discrete case) and 2D conducting medium (continuous case).

- Cracks can be detected in a numerical simulation, in accord with several previous reports.
- Cracks are also well detected in *discrete* and *continuous* media involving actual (noisy) experiments, without introducing artifacts.
- Preliminary experiments have shown that *more than one crack* can be simultaneously detected. However, the limitations of the detection process have not been fully assessed here.

Appendix A. Kirchoff's theorem and its relation to Laplace equation

According to Ohm's law, the electrical current through every resistor (Fig. 14) is the potential difference between the two nodes from his sides, divided by its resistance value. The current direction is arbitrary. Kirchoff's law for electrical net of resistors, which is being applied on every node from the net, positioned at row i and column j, is

$$\sum I_{(i,j)} = Iy_{i,j} + Ix_{i,j-1} + Iy_{i-1,j} + Ix_{i,j} = 0 \qquad \text{(A1)}$$

as current which is directed into a node gets a positive value and the opposite direction gets a negative value. On one

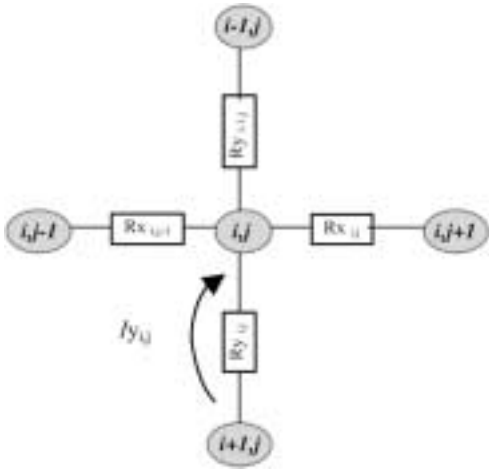

Fig. 14. A single node from a network of resistors net with its surroundings.

node positioned at (i,j), having four resistors in connection, we get

$$\rho(V_{i+1,j} + V_{i-1,j} + V_{i,j+1} + V_{i,j-1} - 4V_{i,j}) = 0 \quad \text{(A2)}$$

V is the electrical potential, I is the electrical current, ρ is the electrical conductance.

The similarity between Eqs. (A2) and (5) with a unit difference ($h = 1$) is related to the finite difference scheme adopted to represent Laplace's equation. This similitude allows us to implement Kirchoff's law on the solution of the problem at hand.

Appendix B. Extending the problem to a 3D domain

For a 3D domain, the node (i,j) of Fig. 14 becomes a 3D node (i,j,k) with six other nodes surrounding it. Extending the 2D case of Eq. (A2) would result as adding two more terms:

$$\rho(V_{i+1,j,k} + V_{i-1,j,k} + V_{i,j+1,k} + V_{i,j-1,k} + V_{i,j,k+1} + V_{i,j,k-1} - 6V_{i,j,k}) = 0 \quad \text{(A3)}$$

The number of nodes providing an algebraic equation each (to Eq. (6) and to all the process) would increase to $m \times n \times l$, where l is the number of nodes on the 3rd dimension.

Similarly, the number of resistors (N) would increase to

$$N = l(2mn - m - n) + mn(l - 1) = 3mnl - mn - ml - nl \quad \text{(A4)}$$

The algorithm would remain basically the same.

Appendix C

C.1. Experimental measurements and process results for Fig. 9

Measured potential on each boundary node. The boldface figure indicates the prescribed potential. Each table represents one set of measurements (Tables A1–A3).

Table A1

8.9400	9.3500	10.2500	11.8700	**14.8700**	12.6000	11.7500
8.5300	–	–	–	–	–	10.9100
7.8100	–	–	–	–	–	9.7600
6.8300	–	–	–	–	–	8.5900
5.6200	–	–	–	–	–	7.5700
3.8800	–	–	–	–	–	6.7700
2.9500	2.0100	**0**	3.1800	4.9200	5.8900	6.3300

Table A2

7.1800	6.8600	6.2800	5.4700	4.5200	3.5200	2.7700
7.4900	–	–	–	–	–	2.0200
8.1500	–	–	–	–	–	**0**
9.2800	–	–	–	–	–	2.9100
11.2000	–	–	–	–	–	4.5500
14.8900	–	–	–	–	–	5.5100
13.3500	11.8300	9.9900	8.4400	7.2500	6.4100	5.9600

Table A3

2.6900	3.4000	4.2200	4.9200	5.8900	6.0900	6.2000
1.8900	–	–	–	–	–	6.3100
0	–	–	–	–	–	6.5400
4.7900	–	–	–	–	–	6.8600
9.0100	0	–	–	–	–	7.2100
14.8600	–	–	–	–	–	7.5200
13.3700	11.8800	10.1500	8.9700	8.2600	7.8700	7.6900

Table A4

$\rho x =$					
2.3792	2.2942	2.0452	1.6518	2.1147	2.0609
2.0108	1.9074	1.7019	1.8168	1.9533	2.0934
1.9517	1.8072	2.0525	2.3089	2.2263	2.0795
1.9966	2.2759	2.5111	2.5356	2.2953	2.0381
1.5206	2.0591	2.5072	2.5067	2.3222	2.1613
2.8739	1.5858	2.0119	2.3169	2.3198	2.2550
2.4338	2.2694	2.4890	2.4292	2.3778	2.2949

Table A5

$\rho y =$						
2.1982	2.0624	1.4886	1.0908	2.7648	2.2081	2.0607
2.3361	1.5906	1.5288	1.8547	2.5410	2.4136	2.0534
2.0580	1.8586	2.1011	2.3810	2.5474	2.3526	2.2140
1.9296	1.9325	2.2747	2.5183	2.5139	2.3424	2.2377
1.6543	0.8397	1.5908	2.3272	2.3917	2.3124	2.2526
2.4235	1.3148	1.6452	2.1673	2.2513	2.2684	2.3025

The value of the error function reduces in the following process from 0.000196838 in optimization step number 1, to 0.000028322 in optimization step number 350.

Results presented in Fig. 9, after 350 optimization steps (all dimensions in $[10^{-3}/\Omega]$) (Tables A4 and A5).

C.2. Experiment measurements and process results for Fig. 10

Measured potential on each boundary node. The boldface

Table A6

6.7300	6.8700	7.6200	9.1400	**14.5000**	9.5400	8.7800	8.4800	8.4000
6.5300	–	–	–	–	–	–	–	8.3300
5.8800	–	–	–	–	–	–	–	8.1300
4.5500	–	–	–	–	–	–	–	7.8400
0	–	–	–	–	–	–	–	7.5600
3.8100	–	–	–	–	–	–	–	7.3200
4.6500	–	–	–	–	–	–	–	7.1800
4.7900	4.9200	5.3400	5.8500	6.3500	6.7000	6.9600	7.1100	7.1500

Table A7

7.9200	7.8900	7.7100	7.3900	6.9400	6.2800	5.6400	5.0700	4.8600
7.9600	–	–	–	–	–	–	–	4.6900
8.1100	–	–	–	–	–	–	–	3.7800
8.3500	–	–	–	–	–	–	–	**0**
8.6900	–	–	–	–	–	–	–	4.5300
9.0100	–	–	–	–	–	–	–	6.3000
9.3000	–	–	–	–	–	–	–	7.2000
9.3800	9.4500	9.7800	10.6900	**14.5900**	10.0700	8.4400	7.5900	7.3600

Table A8

8.1000	8.0600	7.8900	7.6300	7.3200	6.9800	6.7200	6.5400	6.4900
8.1400	–	–	–	–	–	–	–	6.4400
8.3000	–	–	–	–	–	–	–	6.2600
8.6200	–	–	–	–	–	–	–	5.8800
9.2000	–	–	–	–	–	–	–	5.2500
10.0800	–	–	–	–	–	–	–	4.2400
11.7500	–	–	–	–	–	–	–	2.7270
12.7900	**14.6400**	10.4300	8.6800	7.2200	5.8700	4.1100	**0**	2.0240

Table A9

11.4100	11.1000	10.2200	9.4900	9.0300	8.7000	8.5400	8.4300	8.4200
11.7200	–	–	–	–	–	–	–	8.3900
14.5700	–	–	–	–	–	–	–	8.3300
10.1700	–	–	–	–	–	–	–	8.2100
7.8400	–	–	–	–	–	–	–	8.0800
5.7000	–	–	–	–	–	–	–	7.9400
0	–	–	–	–	–	–	–	7.8600
2.8300	3.9100	5.6200	6.6100	7.2100	7.5300	7.7200	7.8100	7.8400

Table A10

6.9600	6.9400	6.8500	6.6400	6.3400	5.7600	5.0300	4.1400	3.7400
6.9800	–	–	–	–	–	–	–	3.3300
7.0500	–	–	–	–	–	–	–	**0**
7.1600	–	–	–	–	–	–	–	5.5800
7.3000	–	–	–	–	–	–	–	8.9000
7.4200	–	–	–	–	–	–	–	**14.5000**
7.5200	–	–	–	–	–	–	–	11.1100
7.5400	7.5600	7.6600	7.8500	8.2000	8.7300	9.5000	10.4100	10.7900

Table A11

$\rho x =$							
1.6964	0.7076	0.5968	0.3599	0.2852	0.7074	0.7910	1.2820
1.8621	0.9624	0.9222	1.5517	1.6784	0.9967	0.9226	1.6477
1.0446	0.9846	1.1510	1.3825	1.4346	1.1777	1.1890	1.2707
1.8978	1.3724	1.3296	1.3475	1.2929	1.1067	1.0015	1.4163
1.1924	1.2954	1.3540	1.3263	1.1928	0.9756	1.1145	1.9739
2.0005	1.2656	1.2033	1.3154	1.1899	0.8346	1.1332	1.2786
1.2435	1.7270	0.9832	1.4747	1.5529	0.9708	1.6457	1.8847
0.3630	0.3616	0.5573	0.3874	0.4490	0.6446	0.4189	0.7282

figure indicates the prescribed potential. Each table represents one set of measurements (Tables A6–A10).

The value of the error function reduces in the following process from 0.00848914 in optimization step number 1, to 0.000782303 in optimization step number 2000.

Results presented in Fig. 10, after 2000 optimization steps (all dimensions in $[10^{-3}/\Omega]$) (Tables A11 and A12).

C.3. Experiment measurements and process results for Fig. 11

Measured potential on each boundary node. The boldface figure indicates the prescribed potential. Each table represents one set of measurements (Tables A13–A15).

Table A12

$\rho y =$								
1.6204	1.2949	1.2899	1.6837	0.7717	1.7870	1.3119	1.2480	1.2983
0.5675	1.4151	1.3262	1.4316	1.4009	1.4815	1.3703	1.6372	0.5088
0.4343	1.2885	1.3707	1.4372	1.4289	1.3986	1.3539	1.6485	0.3449
0.3207	1.3871	1.4158	1.4683	1.4158	1.2941	1.1396	1.2376	0.4351
0.3395	1.2672	1.3513	1.4718	1.3904	1.2237	0.9964	1.2006	0.4251
0.2118	1.6608	1.2816	1.5300	1.4148	1.4218	1.3404	1.4719	0.4257
0.2592	1.2803	1.7681	1.8906	1.2783	1.9326	1.8378	0.9396	1.9462

Table A13

8.6600	9.1000	10.0600	11.7800	**14.9300**	12.6000	11.7200
8.2400	–	–	–	–	–	10.8500
7.4600	–	–	–	–	–	9.7000
6.4400	–	–	–	–	–	8.5200
5.2600	–	–	–	–	–	7.4800
4.0800	–	–	–	–	–	6.6900
3.2080	2.3270	**0**	3.1470	4.8600	5.8200	6.2500

Table A14

7.5500	7.2500	6.6000	5.7300	4.7200	3.6700	2.8870
7.8800	–	–	–	–	–	2.1030
8.5800	–	–	–	–	–	**0**
9.7500	–	–	–	–	–	2.9760
11.6500	–	–	–	–	–	4.6300
14.8800	–	–	–	–	–	5.5900
13.2200	11.5700	9.9000	8.4600	7.3200	6.4900	6.0400

Table A15

2.8380	3.5800	4.4300	5.1200	5.6100	5.9000	6.0400
2.1040	–	–	–	–	–	6.1800
0	–	–	–	–	–	6.4400
5.1600	–	–	–	–	–	6.7800
9.5400	–	–	–	–	–	7.1300
14.8400	–	–	–	–	–	7.4400
13.0800	11.3000	9.7800	8.7600	8.1200	7.7600	7.6000

C.4. Experiment measurements and process results for Figs. 12 and 13

Measured potential on each boundary node. The boldface figure indicates the prescribed potential. Each table represents one set of measurements (Tables A13–A15).

The value of Error function reduces in the following process from 12.9992×10^{-6} in optimization step number 1, to 3.911058×10^{-6} in optimization step number 350.

Results presented in Fig. 11, after 350 optimization steps (all dimensions in $[10^{-3}/\Omega]$) (Tables A16 and A17).

Table A16

$\rho x =$					
2.1445	2.0952	2.1132	2.1044	2.1065	2.0900
2.1331	2.1471	2.1110	2.1353	2.1605	2.1829
2.1284	2.1464	2.1152	2.1086	2.1148	2.0902
2.1535	2.1286	2.1037	2.0925	2.0974	2.1631
2.0892	2.1216	2.1062	2.0915	2.0823	2.0962
2.1544	2.1626	2.1454	2.1193	2.1096	2.1090
2.1248	2.1259	2.1259	2.1402	2.1374	2.1567

Table A17

$\rho y =$						
2.1491	2.2004	2.1249	2.1187	2.1463	2.1192	2.1033
2.1445	2.2089	2.1535	2.1278	2.1634	2.2107	2.1420
2.1334	2.1727	2.1353	2.1159	2.1237	2.1517	2.1245
2.1311	2.1136	2.1130	2.0977	2.0877	2.0875	2.1411
2.1287	2.0961	2.1284	2.1101	2.1020	2.0997	2.1330
2.1350	2.1352	2.1099	2.1519	2.1434	2.1352	2.1247

Table A18

0	5.5600	9.8900	**14.8100**	12.9000	12.2100	11.8800
4.4500	–	–	–	–	–	11.5500
6.6100	–	–	–	–	–	10.9200
7.7300	–	–	–	–	–	10.4600
8.3300	–	–	–	–	–	10.2400
8.6300	–	–	–	–	–	10.0500
8.7700	8.8800	9.1200	9.4100	9.6900	9.8800	9.9600

Table A19

8.8200	8.6700	8.3000	7.6800	6.2500	3.9200	**0**
9.0100	–	–	–	–	–	5.2400
9.3000	–	–	–	–	–	10.2300
9.5800	–	–	–	–	–	**14.8600**
9.8300	–	–	–	–	–	13.0900
10.0200	–	–	–	–	–	12.3200
10.1200	10.2300	10.4400	10.7800	11.2500	11.7000	12.0100

Table A20

10.3000	10.2100	10.0900	9.8500	9.5300	9.2900	9.1100
10.4400	–	–	–	–	–	8.9300
10.6300	–	–	–	–	–	8.4400
10.9300	–	–	–	–	–	7.7300
11.3000	–	–	–	–	–	6.5400
11.6900	–	–	–	–	–	4.4000
11.9800	12.2700	13.0200	**14.8400**	9.8500	5.4900	0

Table A21

11.8300	11.5300	11.1300	10.8300	10.5000	10.3400	10.2300
12.1200	–	–	–	–	–	10.1400
12.9000	–	–	–	–	–	9.8500
14.8300	–	–	–	–	–	9.5900
9.9200	–	–	–	–	–	9.3200
5.5600	–	–	–	–	–	9.0800
0	4.4900	6.6900	7.8200	8.4300	8.7500	8.8700

Table A22

$\rho x =$					
0.1521	0.1610	0.1520	0.1288	0.1443	0.1383
0.1384	0.1336	0.1628	0.1083	0.1062	0.1698
0.1427	0.1485	0.1812	0.1548	0.0771	0.1130
0.1451	0.1031	0.1070	0.1280	0.1467	0.1527
0.1827	0.1470	0.0667	0.1108	0.0920	0.1322
0.1417	0.1624	0.1196	0.0817	0.1107	0.1347
0.1409	0.1392	0.1427	0.1511	0.1519	0.1460

Table A23

$\rho y =$						
0.1440	0.1250	0.1132	0.1510	0.1357	0.0912	0.1265
0.1482	0.1085	0.1160	0.1286	0.0919	0.0625	0.1009
0.1396	0.1702	0.1674	0.1545	0.0930	0.1235	0.1153
0.1521	0.1111	0.1637	0.1324	0.1419	0.1700	0.1349
0.1466	0.1468	0.1245	0.1588	0.0751	0.1143	0.1398
0.1472	0.1393	0.1507	0.1213	0.1494	0.1368	0.1328

Table A24

$\rho x =$					
0.1402	0.1554	0.1400	0.1151	0.1202	0.1234
0.1437	0.0863	0.1758	0.0842	0.1533	0.1217
0.1297	0.1447	0.1689	0.1712	0.0626	0.1030
0.1598	0.0729	0.0608	0.1519	0.1751	0.1266
0.1936	0.1453	0.0301	0.0878	0.0487	0.1445
0.1264	0.1795	0.1404	0.0746	0.0859	0.1403
0.1284	0.1244	0.1267	0.1409	0.1438	0.1318

Table A25

$\rho y =$						
0.1293	0.1190	0.1004	0.1427	0.1331	0.0963	0.1174
0.1329	0.0861	0.1314	0.0758	0.0772	0.0319	0.1040
0.1242	0.1541	0.1687	0.1610	0.1305	0.0943	0.1125
0.1245	0.1375	0.1416	0.1412	0.1736	0.1415	0.1233
0.1238	0.1580	0.0830	0.1526	0.0687	0.1067	0.1234
0.1318	0.1164	0.1305	0.1032	0.1412	0.1172	0.1212

figure indicates the prescribed potential. Each table represents one set of measurements (Tables A18–A21).

The value of Error function reduces in the following process from 1.57819 in optimization step number 1, to 0.0991329 in optimization step number 100.

Results presented in Fig. 12, after 100 optimization steps (all dimensions in $[10^{-3}/\Omega]$) (Tables A22 and A23).

The value of error function reduces in the following process from a value of 0.0902686 in optimization step number 200, into a value of 0.0868226 in optimization step number 300.

Results presented in Fig. 13, after 300 optimization steps (all dimensions in $[10^{-3}/\Omega]$) (Tables A24 and A25).

References

[1] McGraw-Hill multimedia encyclopedia of science and technology. version 2.0, The McGraw-Hill Companies, Inc., 1998. Software development: TechBooks, Fairfax, VA.

[2] Friedman A, Vogelius M. Determining cracks by boundary measurements. Indiana Univ Math J 1989;38(3):527–55.

[3] Santosa F, Vogelius M. A computational algorithm to determine cracks from electrostatic boundary measurements. Int J Engng Sci 1991;29(N8.0):917–37.

[4] Nishimura N, Kobayashi S. A boundary integral equation method for an inverse problem related to crack detection. Int J Numer Meth Engng 1991;32:1371–87.

[5] Andrieux S, Abda AB. The reciprocity gap: a general concept for flaws identification problems. Mech Res Commun 1993;20(5):415–20.

[6] Mellings SC, Aliabadi MH. Dual boundary element formulation for inverse potential problems in crack identification. Engng Anal Bound Element 1993;12:275–81.

[7] Mellings SC, Aliabadi MH. Flaw identification using the boundary element method. Int J Numer Meth Engng 1995;38:399–419.

[8] Dobson DC, Santosa F. An image-enhancement technique for electrical impedance tomography. Inverse Problem 1994;10(2):317–34.

[9] Alessandrini G. Stable determination of a crack from boundary measurements. Proc R Soc Edinburgh 1993;123A:497–516.
[10] Kaup PG, Santosa F. Nondestructive evaluation of corrosion damage using electrostatic measurements. J Nondestruct Eval 1995; 14(3):127–36.
[11] Santosa F. Applications of electrical impedance tomography to nondestructive evaluation. Design Engineering Technical Conferences—part C, vol. 3. ASME, 1995. p. 931–7.
[12] Dines KA, Lytle RJ. Analysis of electrical conductivity imaging. Geophysics 1981;46(7):1025–36.
[13] Liepa V, Santosa F, Vogelius M. Crack determination from boundary measurements—reconstruction using experimental data. J Nondestruct Eval 1993;12(3):163–74.
[14] Barber DC, Brown BH. Progress in electrical impedance tomography. In: Colton D, et al., editors. Inverse problems in partial differential equations, Philadelphia, PA: SIAM Publications, 1990. p. 151–64.
[15] Santosa F, Vogelius M. A backprojection algorithm for electrical impedance imaging. SIAM J Appl Math 1990;50(1):216–43.
[16] Mellings SC, Aliabadi MH. Crack identification using inverse analysis. Stress Analysis Proceedings of the International Conference on Boundary Element Methods BEM XV, Computational Mechanics Publishers, 1993. p. 261–73.
[17] Tychonov AN, Samarski AA. Partial differential equations of mathematical physics, vol. I. San Francisco, CA: Holden-Day Inc, 1964. p. 325–30.
[18] Cheney M, Isaacson D, Newell JC. Electrical impedance tomography. SIAM Rev 1999;41(1):85–101.
[19] Santosa F. Inverse problem holds key to safe, continuous imaging. SIAM News 1994;27(6):1–18.
[20] Johnson CR. Direct and inverse bioelectric field problems. In: Umar V, editor. Computational science education project (CSEP), Washington, DC: DOE, 1994.
[21] Sigmon K. MATLAB primer. 2nd ed. Department of Mathematics, University of Florida, Gainesville, FL, 1992.
[22] MATLAB optimization toolbox user's guide, Natick, MA: The MATHWORKS, 1998.
[23] Han SP, Globally A. Convergent method for nonlinear programming. J Optimiz Theor Applic 1977;22:297–309.
[24] Gill PE, Murray W, Wright MH. Practical optimization. London: Academic Press, 1981. p. 176–80.
[25] Shanno DF. Conditioning of quasi-Newton methods for function minimization. Math Comput 1970;24:647–56.